energies

MDPI

Article

Enhanced Aqueous Zinc-Ion Batteries Using 3D MoS_2/Conductive Polymer Composite

Tongxin Jiang [1,†], Sijie Li [2,†], Zexiang Luo [1], Xue Li [2], Lifeng Zhang [2], Haisheng San [1,*], Xin Li [2,*] and Yifei Ma [3,*]

[1] Pen-Tung Sah Institute of Micro-Nano Science and Technology, Xiamen University, Xiamen 361005, China; jiangtongxin@stu.xmu.edu.cn (T.J.); luozexiang@stu.xmu.edu.cn (Z.L.)
[2] China Institute of Atomic Energy, Beijing 102413, China; 05hgygylsj@163.com (S.L.); li_xue1102@163.com (X.L.); zhanglifeng@ciae.ac.cn (L.Z.)
[3] State Key Laboratory of Quantum Optics and Quantum Optics Devices, Institute of Laser Spectroscopy, Collaborative Innovation Center of Extreme Optics, Shanxi University, Taiyuan 030006, China
* Correspondence: sanhs@xmu.edu.cn (H.S.); lixin_0128@sina.com (X.L.); mayifei@sxu.edu.cn (Y.M.)
† Those authors contributed equally to this work.

Abstract: MoS_2, a typical transition metal dichalcogenide, features a layered structure, multi-phase transition, and tunable band gap, which is a promising candidate for aqueous zinc-ion batteries (AZIBs). Recent studies have focused on the metastable 1T-MoS_2 phase, which exhibits superior electrical conductivity and electrochemical activity compared to the more stable 2H phase. Herein, a straightforward one-step hydrothermal method was used to synthesize three-dimensional MoS_2/polymer composites (H-MoS_2-PEDOT). Under acidic conditions, the polymerization and intercalation of EDOT molecules in the MoS_2 layers promote the phase transition from 2H to 1T, thereby enhancing its conductivity and electrochemical performance. Additionally, it was found that the intercalated PEDOT and small amounts of water molecules have contributed to enhancing Zn^{2+} ion diffusion and cycle stability. As a result, AZIBs based on the H-MoS_2-PEDOT composite deliver a high specific capacity of 173.6 mAh g^{-1} at 1 A g^{-1}, maintaining a specific capacity of 116 mAh g^{-1} and a capacity retention of 82.8% after 1000 cycles at 5 A g^{-1}.

Keywords: aqueous zinc-ion battery; MoS_2; PEDOT; molecular intercalation; reaction kinetics

Academic Editors: Chenggang Wang, Lu Wang and Xiaoyu Luan

Received: 5 December 2024
Revised: 21 December 2024
Accepted: 23 December 2024
Published: 25 December 2024

Citation: Jiang, T.; Li, S.; Luo, Z.; Li, X.; Zhang, L.; San, H.; Li, X.; Ma, Y. Enhanced Aqueous Zinc-Ion Batteries Using 3D MoS_2/Conductive Polymer Composite. *Energies* **2025**, *18*, 34. https://doi.org/10.3390/en18010034

1. Introduction

Lithium-ion batteries (LIBs) have undergone substantial commercial growth due to their extended cycle life, high energy density, and compact design [1–5]. However, LIBs face significant challenges due to the limited availability of lithium resources and safety concerns related to the flammability of their electrolytes [6,7]. These limitations have driven the exploration of alternative, sustainable, and environmentally friendly energy storage technologies. Among these, aqueous zinc-ion batteries (AZIBs) have attracted considerable attention owing to their inherent advantages [8–12], such as abundant zinc resources, non-toxic aqueous electrolytes, high energy density, and excellent cycle stability [13–15]. AZIBs are considered a practical and cost-effective solution for a wide range of energy storage applications, especially in the context of sustainable energy and carbon-neutral strategies.

The zinc anode has a theoretical capacity of 820 mAh g^{-1} and a lower electrode potential [16]. However, the development of high-performance cathode materials is critical to fully exploit the potential of ZIB anodes. In the research for cathode materials, layered materials such as manganese oxides (MnO_2 [17], Mn_3O_4 [18], δ-MnO_2 [19], etc.) and

vanadium oxides (V_2O_5 [20], VO_2 [21,22], V_2O_3 [23], etc.) have been widely studied for their promising electrochemical performance.

In recent years, MoS_2, a typical transition metal dichalcogenide (TMDC), has become a potential cathode material for AZIBs owing to its distinctive layered structure with an interlayer spacing of approximately 0.62 nm and excellent conductivity [24,25]. However, bulk MoS_2 in its natural 2H phase has low electrical conductivity and discharge capacity (18 mA h g^{-1}) [26,27]. It could be attributed to the robust electrostatic interactions between the intercalated Zn^{2+} ions and the host framework [28]. To overcome these challenges, several strategies have been used to modify MoS_2, including defect introduction [29], nanostructure tailoring [24], and coupling with highly conductive matrices [27]. Additionally, by introducing guest ions or heterostructures, the semiconducting character of the 2H phase can be effectively converted to the metallic 1T phase [30,31]. The shift of MoS_2 from 2H to 1T phase has been verified to enhance its electrical conductivity and electrochemical performance, rendering it a potential candidate for high-performance AZIBs [28,32]. Recent studies have demonstrated that incorporating Co ions and water molecules into MoS_2 can effectively increase the interlayer spacing and facilitate the phase transition to 1T MoS_2, resulting in enhanced electrochemical properties [33]. Liu et al. demonstrated that the insertion of Co ions and the introduction of water molecules could achieve a volumetric capacity of 305.4 mAh cm^{-3} at 0.1 A cm^{-3}, significantly improving the electrochemical properties of MoS_2-based cathodes [34]. Similarly, Yang et al. developed an Mn-intercalated MoS_2 composite, which not only maintained a stable 1T phase but also enhanced the interlayer spacing, achieving a specific capacity of 191.7 mAh g^{-1} at 0.1 A g^{-1} and a capacity retention of 80.3% over 500 cycles at 1 A g^{-1} [35]. The comparison of relevant research works is shown in Table S1 in Supplementary Material. Despite these improvements, MoS_2-based cathodes still fail to meet the commercial standards for capacity and cycling stability, indicating the need for further optimization.

In this work, a three-dimensional MoS_2/conductive material polymer composite (H-MoS_2-PEDOT) was prepared using a simple one-step hydrothermal method under acidic conditions. The acidic environment accelerated the polymerization of EDOT molecules [36]. The intercalation of PEDOT molecules not only expanded the interlayer spacing of molybdenum disulfide and enhanced its conductivity but also facilitated the phase transition from 2H to 1T [37]. In addition, some water molecules can be infiltrated into the molybdenum disulfide layer, resulting in the generation of oxygen defects and an increase in the ion diffusion rate. As a result, H-MoS_2-PEDOT/Zn batteries gained a specific electrochemical capacity of 173.6 mAh g^{-1} at 1 A g^{-1}, maintaining a specific capacity of 116 mAh g^{-1} and a capacity retention of 82.8% after 1000 cycles at 5 A g^{-1}.

2. Methods and Materials

2.1. Materials Preparation

Three-dimensional MoS_2/conductive material polymer composites were fabricated using a simple one-step hydrothermal method. For comparison, commercial bulk MoS_2, samples without EDOT ($MoS_2 \cdot H_2O$), and samples without hydrochloric acid (MoS_2-PEDOT) were also synthesized.

Bulk MoS_2: Bulk MoS_2 used was commercial products (Sigma-Aldrich, Darmstadt, Germany).

Bulk $MoS_2 \cdot H_2O$: Ammonium molybdate tetrahydrate (99%, Damas-beta, Shanghai, China) and thiourea (99%, Macklin, Shanghai, China) (mass ratio 1:2) were mixed with 75 mL of deionized (DI) water. The solution was thoroughly mixed and then placed in a Teflon-lined stainless-steel autoclave and heated at 180 °C for 24 h. The resulting black

precipitate was washed with DI water and anhydrous ethanol and subsequently dried at 60 °C for 12 h to eliminate any residual solvents (the hydrothermal method).

MoS_2-PEDOT: Ammonium molybdate tetrahydrate (Damas-beta, 99%) and thiourea (Macklin, 99%) (mass ratio 1:2) were mixed with 75 mL of DI water. After the solution was thoroughly mixed, add 20 µL 3,4-ethylenedioxythiophene (EDOT, 99.0%, Urchem, Shanghai, China) in this mixed solution. Continue stirring for 30 min. The hydrothermal process mentioned above for Bulk $MoS_2 \cdot H_2O$ was then repeated.

H-MoS_2-PEDOT: Ammonium molybdate tetrahydrate (Damas-beta, 99%) and thiourea (Macklin, 99%) (mass ratio 1:2) were mixed with 75 mL of DI water. After the solution was thoroughly mixed, add 20 µL 3,4-ethylenedioxythiophene (EDOT, Urchem, 99.0%) and 1 mL Hydrochloric acid in this mixed solution. Continue stirring for 30 min. The hydrothermal process mentioned above for Bulk $MoS_2 \cdot H_2O$ was then repeated.

2.2. Materials Characterization and Testing

X-ray diffraction (XRD) images were obtained using a SHIMADZU XRD-7000 (Kyoto, Japan), with the 2θ angle ranging from 5 to 80°. Scanning electron microscopy (SEM) images were acquired using the ZEISS SUPRA55 SAPPHIRE (Oberkochen, Germany). Transmission electron microscope (TEM) images and energy dispersive X-ray spectroscopy (EDS) element mapping were obtained with a copper mesh grid as the substrate (FEI Talos F200S microscope, MA, USA). X-ray photoelectron spectroscopy (XPS) data were collected using a Thermo Scientific K-Alpha (Waltham, MA, USA) spectrometer equipped with a monochromatic Al Kα X-ray source. Thermogravimetric (TG) were tested in an N_2 atmosphere at a temperature range from 30 °C to 790 °C using the Discovery TGA-5500 Thermogravimetric Analyzer (DE, USA). Fourier transform infrared spectroscopy (FTIR) was collected using a NICOET iS10 (Thermo Scientific, Waltham, MA, USA) instrument.

The active materials, acetylene black and polyvinylidene fluoride (PVDF), were dissolved in N-methyl-2-pyrrolidone at a mass ratio of 7:2:1. The resulting mixture was cast onto titanium foil and dried under vacuum at 100 °C for 12 h. The active materials were loaded onto the titanium foil with an average mass of approximately 1.5–2.1 mg cm^{-2}. The AZIBs were assembled as 2032-type coin cells, with metallic zinc foil as the counter electrode and 3M $Zn(CF_3SO_3)_2$ solution as the electrolyte. Discharge/charge tests and cyclic voltammograms (CV) were tested in a potential range of 0.2–1.4 V using a LANHE Testing System (G340A, LANHE, Wuhan, China). Electrochemical impedance spectra (EIS) were measured using a DH700 impedance analyzer (Donghua, Shanghai, China).

3. Results and Discussion

The XRD pattern, as shown in Figure 1a, revealed that the bulk MoS_2 diffraction peaks are aligned with the standard diffraction peaks PDF#37-1492 (2H MoS_2). However, the diffraction peaks of other samples exhibited a little offset. According to the Bragg equation, the material layer spacing can be determined [38]. Specifically, the $MoS_2 \cdot H_2O$ layer spacing was found to be 7.5 Å, attributed to the intercalation of water molecules. In contrast, the larger atomic radius of organic polymers further expanded the layer spacing, with the H-MOS_2-PEDOT layer spacing reaching 9.5 Å under acidic conditions. As different guest molecules were deeply embedded, MoS_2 underwent a gradual phase transition from 2H to 1T, which corresponded to the observed offsets in the XRD peak [39]. The 1T metal phase is known for its good electrical conductivity and electrochemical activity, thus enhancing the overall electrochemical performance of the materials [40]. The chemical composition and morphological transformation of the samples were further investigated using SEM, HRTEM, and EDS element mapping, respectively. Figure 1b displays the SEM image and EDS mapping of H-MoS_2-PEDOT, revealing a lamellar 3D network structure of MoS_2. The

elements S, Mo, and O were evenly distributed in the hybrid, confirming the effective combination of PEDOT with MoS_2. Additionally, SEM images and EDS mapping of other samples are presented in Figures S1–S3, clearly showing the morphological change from a blocky structure to a 3D network structure after the intercalation of guest molecules. The elements S, Mo, and O were uniformly arranged in each sample. SEM images with the same magnification are shown in Figure S4. It can be observed that the intercalation of water molecules and the H-MoS_2-PEDOT have the smallest grain size compared to others, along with a uniform distribution. This small grain size is beneficial for improving electrochemical performance [40]. The morphology of H-MoS_2-PEDOT was further analyzed using TEM, as shown in Figure 1c,d. Under high magnification, it is verified that the primary particles consist of nanoscale fibrous structures. The elements S, Mo, O, and C were uniformly distributed in the composite. The HRTEM image, as shown in Figure 1d, reveals that the lattice spacing corresponding to the 002 crystal faces was 0.949 nm, which is consistent with the XRD results.

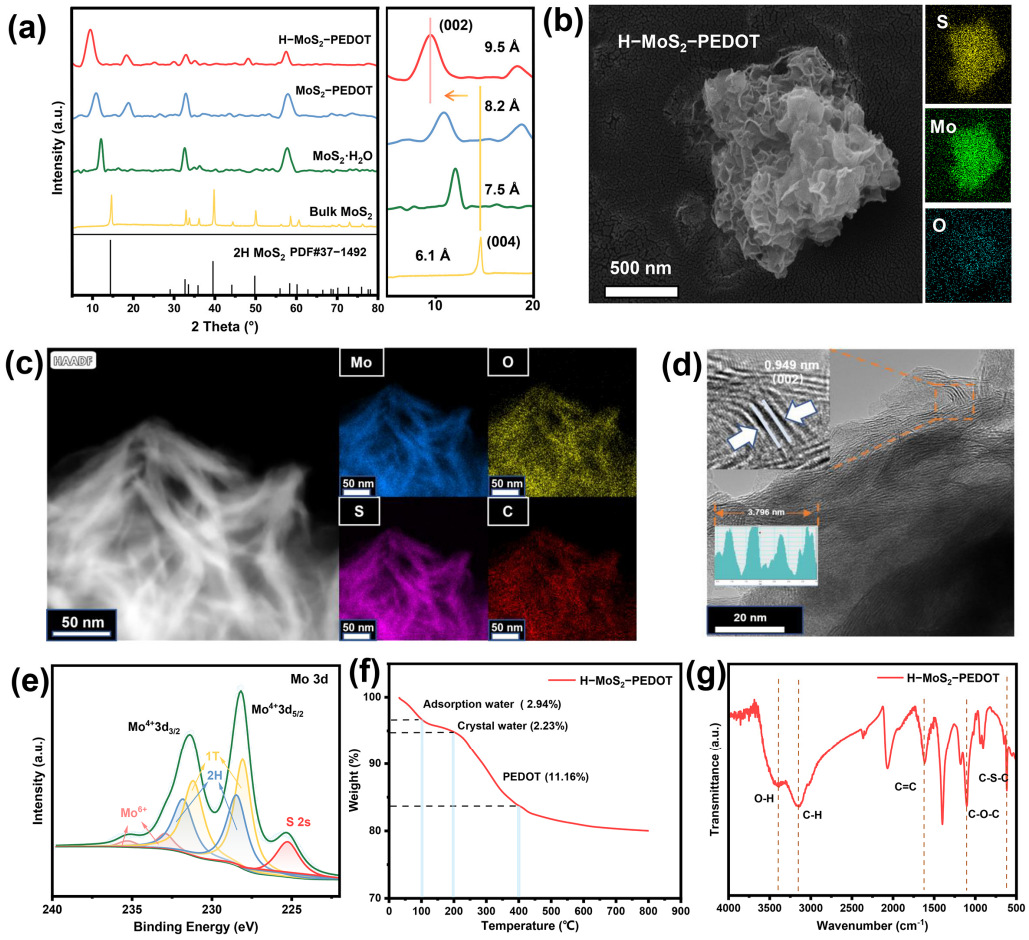

Figure 1. Material characterizations of H-MoS_2-PEDOT. (**a**) XRD patterns; (**b**) SEM images with EDS mapping images; (**c**) TEM patterns with EDS mapping images; (**d**) HRTEM image; (**e**) XPS spectrum; (**f**) TG curves; and (**g**) FTIR spectrum.

Furthermore, Figure 1e and Figure S5 displayed the XPS spectra of H-MoS_2-PEDOT composites, which include the Mo 3d and S 2p peaks. The Mo 3d spectrum exhibited two prominent peaks and two weaker peaks. The two prominent peaks correspond to Mo $3d_{3/2}$ and Mo $3d_{5/2}$, respectively [41]. Specifically, the peaks located at 228.1 eV and 231.3 eV are attributed to Mo^{4+}, while those at 228.7 eV and 231.9 eV are associated with the 2H phase. Additionally, the peaks at 235.4 eV and 233.1 eV are attributed to Mo^{6+} [34]. The presence

of Mo^{6+} is attributed to the intercalation of water molecules. Therefore, H-MoS_2-PEDOT consists of water molecules co-intercalated with PEDOT. The peak at 225.2 eV is corresponded to S 2s [34]. The peaks located at 160.5, 162.3, and 161.4 eV are attributed to S $2p_{1/2}$, S $2p_{3/2}$, and the 1T-phase, respectively. Moreover, the thermogravimetric curve (Figure 1f) illustrates the amount of absorption/crystal water molecules and PEDOT in the H-MoS_2-PEDOT. At temperatures ranging from 20–100 °C and 100 °C to 200 °C, the weight decreased by 2.94% and 2.23%, respectively, which is attributed to the evaporation of adsorption and crystal water. The weight reduction between 200 °C and 400 °C is due to the thermal decomposition of PEDOT. To further confirm the effective intercalation of polymers and water molecules into MoS_2, the FTIR was presented in Figure 1g. Peaks at 621, 1108, 1616, and 3146 cm^{-1} correspond to the symmetric stretching of the C–S–C, C–O–C, C=C, and C–H bonds of PEDOT, respectively [42]. A characteristic peak appears at 3386 cm^{-1}, corresponding to the symmetric stretching of the O–H bond from the intercalated water molecules. The effective introduction of guest molecules is in favor of enhancing the electrochemical performance.

Figure 2 exhibited the electrochemical performance of AZIBs based on the H-MoS_2-PEDOT composite. Figure 2a shows the CV profiles of H-MoS_2-PEDOT at 0.1 mV s^{-1} during the first five cycles, within a potential range of 0.2–1.4 V. Aside from a slightly lower capacity in the first cycle, the remaining cycle curves showed significant overlap, indicating that the AZIBs based on H-MoS_2-PEDOT exhibited excellent cycle stability. During the cycling, five redox peaks were located at approximately 0.4 V, 1.1 V, 1.35 V, 0.75 V, and 0.36 V, respectively, providing additional electrochemical insights. The electrochemical performance of AZIBs based on H-MoS_2-PEDOT at 0.1 A g^{-1} was depicted in Figure S6. The discharge capacities for the 1st, 3rd, 4th, and 5th cycles were 134.9, 237.4, 239.4, and 239.6 mAh g^{-1}, respectively, aligning well with the CV curve. Figure 2b shows the electrochemical cyclic curves of different samples at 1 A g^{-1}. After 50 cycles at 1 A g^{-1}, the capacities of bulk MoS_2, $MoS_2 \cdot H_2O$, MoS_2-PEDOT, and H-MoS_2-PEDOT were 23.5, 122.8, 141.7, and 173.6 mAh g^{-1}, respectively. Bulk MoS_2 demonstrated the lowest specific discharge capacity. The intercalation of guest molecules exhibited different specific discharge capacities. Specifically, the polymer molecular intercalation resulted in a more significant increase in specific discharge capacity compared to water molecular intercalation. Under acidic conditions, PEDOT molecular intercalation achieved the highest specific discharge capacity. It was attributed to the fact that PEDOT can significantly accelerate its polymerization rate under acidic conditions [43]. Furthermore, Figure 2c displays the rate performance of MoS_2. The bulk MoS_2 not only exhibited a low capacity but also poor rate performance. The modified water molecular intercalation demonstrated good magnification performance but a relatively low capacity. Conversely, the intercalation of MoS_2 by PEDOT under normal conditions yielded a higher specific discharge capacity, but its rate performance was unsatisfying. Obviously, H-MoS_2-PEDOT exhibited both a higher discharge capacity and superior rate performance, achieving specific capacities of 39.4, 215.1, 190.5, 175.1, and 134.4 mAh g^{-1} at 0.1, 0.5, 1, 2, and 5 A g^{-1}, respectively. Additionally, Nyquist plots of MoS_2 were presented in Figure 2d. Bulk MoS_2 had the highest resistance, and the resistance reduction was dependent on the intercalation of guest molecules, aligning with the above results. H-MoS_2-PEDOT exhibited the lowest resistance among the samples. The long-term cycling performance of MoS_2 at 5 A g^{-1} was illustrated in Figure 2e. After 1000 cycles of charging and discharging, the capacity retention rates for bulk MoS_2, $MoS_2 \cdot H_2O$, MoS_2-PEDOT, and H-MoS_2-PEDOT were 15.3%, 49.6%, 31.3%, and 82.8%, respectively. H-MoS_2-PEDOT demonstrated excellent cyclic stability and a high specific discharge capacity, being consistent with the previous findings. In comparison with other electrodes, H-MoS2-PEDOT exhibited superior electrochemical performance due to the intercalation of polymer molecules under acidic conditions.

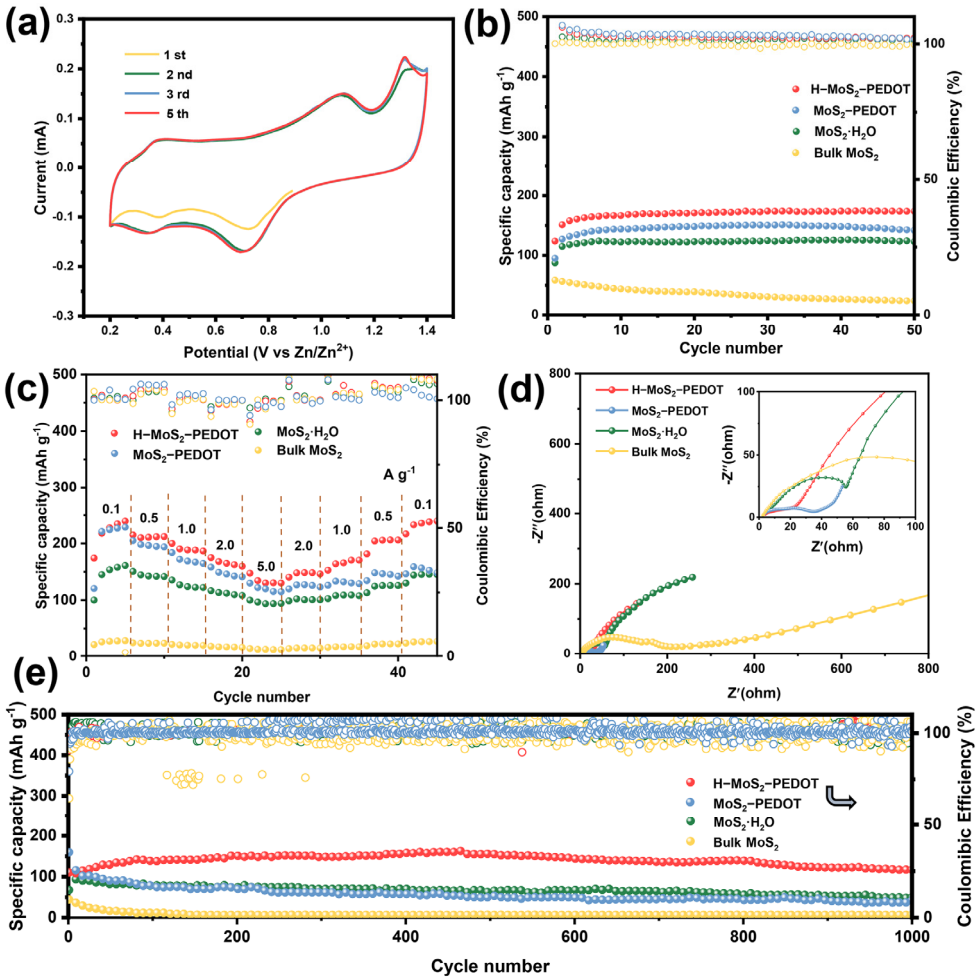

Figure 2. Electrochemical performance of AZIBs based on H-MoS_2-PEDOT composite. (**a**) CV curves at 0.1 mV s^{-1}; (**b**) Electrochemical cycling curves at 1.0 A g^{-1}; (**c**) Rate capability; (**d**) EIS spectra; (**e**) Long-term cycling stability at 5.0 A g^{-1}.

Furthermore, the reaction kinetics were analyzed using the multi-scan CV method and GITT. The electrochemical energy storage analysis of Zn/H-MoS_2-PEDOT batteries is presented in Figure 3. The CV curves were examined at scan rates ranging from 0.1 to 0.8 mV s^{-1} within a potential window of 0.2 to 1.4 V, as depicted in Figure 3a. As the scanning speed increased, the locations of redox peaks did not vary, and the redox peaks were distinctive at various scanning speeds. Typically, the battery capacity is composed of both a pseudo-capacitance-controlled part and a diffusion-controlled part. In general, the relationship between current and voltage in the CV curve can be described as follows [44]:

$$i = av^b \quad (1)$$

In this formula, the values of a and b are variables. When the value of b approaches 0.5, it indicates diffusion control. Whereas, when the value of b approaches 1, it suggests pseudo-capacitance control. The curve obtained from log (i) to log (v) was fitted to determine the b value, as illustrated in Figure 3b. The b values corresponding to the five redox peaks were found to be 0.981, 0.619, 0.620, 0.927, and 0.703, respectively. This implies that the entire cycle process involved both diffusion control and pseudo-capacitance control. Further quantitative analysis was conducted to calculate the contribution rate of pseudo-capacitance as follows [34]:

$$i(v) = k_1 v + k_2 v^{1/2} \quad (2)$$

The diffusion-controlled capacitance and the pseudo-capacitance are represented by $k_1 v$ and $k_2 v^{1/2}$, respectively. By rearranging the aforementioned formula, we obtain the following equation:

$$i(v)/v^{1/2} = k_1 v^{1/2} + k_2 \quad (3)$$

Figure 3c showed the bar chart of the pseudo-capacitance contribution rate. It is evident that as the scan speed was increased from 0.1 to 0.8 mV s^{-1}, the pseudo-capacitance contribution rate gradually raised from 42.3% to 81.2%. The fitting curve of the pseudo-capacitance contribution rate is presented in Figure 3d. The 1st and 4th peaks contributed the main pseudo-capacitance, corresponding to the b values in Figure 3b. Additionally, the zinc ion diffusion rate (D_{Zn}) was further analyzed using the GITT technique, as shown in Figure S7. It was observed that the zinc ion diffusion rate in the cyclic process of MoS_2-PEDOT was 10^{-10} to 10^{-12} cm^2 s^{-1}, while it was 10^{-9}–10^{-11} cm^2 s^{-1} in the cyclic process of H-MoS_2-PEDOT. The insertion of PEDOT under acidic conditions facilitated the acceleration of zinc ion diffusion. Overall, the insertion of the PEDOT polymer under acidic conditions reduce the crystal size and increase the layer spacing, leading to a faster ion diffusion rate and excellent electrochemical performance.

To further investigate the changes in crystal structure during the charging and discharging process, as well as the mechanism of zinc ion desertion/insertion in H-MoS_2-PEDOT, a series of ex-situ tests were conducted. Ex-situ XRD tests, depicted in Figure 4a, revealed that during the charge and discharge cycle, the diffraction peaks at around 10° and 34° were shifted to a smaller angle with the decrease in voltage, and there was no obvious new phase formation in this process. Therefore, the zinc ions were embedded in the interlayers and vacancies. With the increase in voltage, it could be found that the diffraction peaks gradually shifted to the initial position, which was considered as the process of zinc ion desertion. Figure S8 shows the ex-situ SEM images and EDS mapping images. After a full discharging, S, Mo, and Zn elements were evenly distributed in the crystal. However, only a small amount of Zn was observed with a full charge, which is consistent with the XRD results. Additionally, the valence states of the elements were further analyzed using XPS. The ex-situ XPS curves of Mo 3d of H-MoS_2-PEDOT at different states are shown in Figure 4b. The entire Mo element comprises the 1T phase, the 2H phase, and Mo^{6+}. Mo^{6+} binds to water molecules in the material, forming oxygen-supplying defects [32]. After fully discharging, the 2H phase gradually transitions to the 1T phase. It was observed that the structure and electronic properties of Zn^{2+} undergo changes during the Zn^{2+} insertion process, resulting in a transition from the 2H phase to the 1T phase. As the process was turned to a charging state, the 1T phase was shifted to the original 2H phase, indicating that the AZIBs based on H-MoS_2-PEDOT exhibit good electrochemical cycle stability [45]. Furthermore, Figure 4c displays the ex-situ XPS curves of Zn 2p for H-MoS_2-PEDOT at different states. In the initial state, no Zn peak is detected. With full discharging, two signals are observed: Zn^{2+} in the intercalation state and Zn^{2+} on the surface. With full charging, the intercalated zinc ions could be effectively removed, and only surface Zn^{2+} is detected, which is attributed to the residue of the electrolyte. These results are consistent with XRD and SEM findings, suggesting the excellent reversibility of AZIBs based on H-MoS_2-PEDOT.

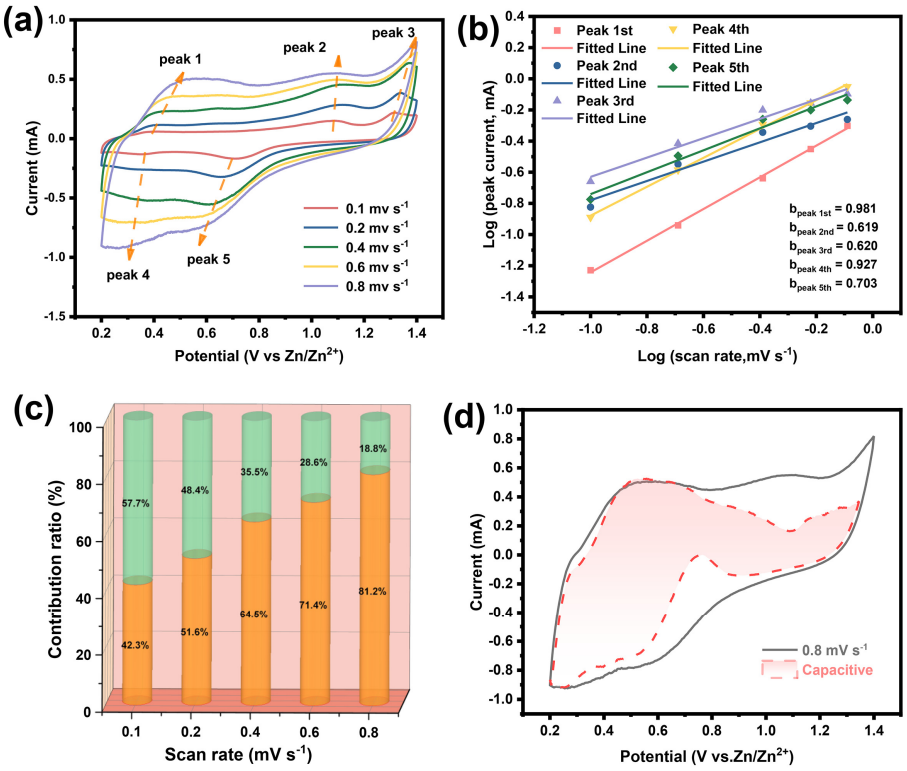

Figure 3. Electrochemical energy storage analysis of H-MoS_2-PEDOT. (**a**) CV curves at various scan rates; (**b**) Logarithmic plots of peak current and scan rates; (**c**) Contributions of pseudo-capacitive (Yellow) and diffusion (Green) processes at different scan rates. (**d**) Capacitive contributions of at 0.8 mV s^{-1}.

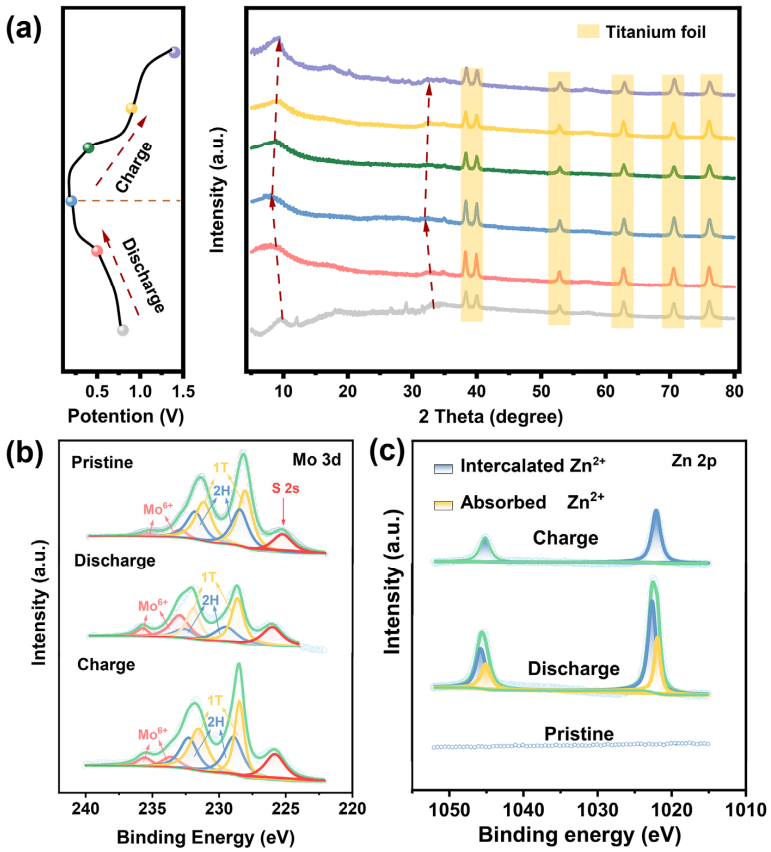

Figure 4. Ex-situ (**a**) XRD images, high-resolution XPS spectra of (**b**) Mo 3d and (**c**) Zn 2p.

4. Conclusions

In summary, H-MoS_2-PEDOT, with high stability and high capacity, was prepared using the hydrothermal method. The intercalation of different guest ions in MoS_2 and acid conditions was analyzed, revealing that the intercalation with different guest molecules increases the layer spacing, and polymers with larger molecular volumes provide greater layer spacing. Compared to normal hydrothermal conditions, acidic conditions promoted the polymerization of EDOT molecules, enabling them to effectively intercalate into MoS_2. The incorporation of PEDOT with MoS_2 not only increased the layer spacing of MoS_2 but also enhanced its conductivity, cycle stability, and Zn^{2+} diffusion rate. As a result, the AZIBs based on H-MoS_2-PEDOT achieved a specific electrochemical cycling capacity of 173.6 mAh g^{-1} at 1 A g^{-1} and demonstrated excellent long-term cycle stability, maintaining a specific capacity of 116 mAh g^{-1} and a capacity retention of 82.8% after 1000 cycles at 5 A g^{-1}. The acidic conditions facilitated polymerization and strengthened the bonding between the polymer and MoS_2, dramatically improving the electrochemical property of AZIBs. It is expected that the AZIBs based on H-MoS_2-PEDOT can become one of the efficient energy storage solutions in the future.

Supplementary Materials: The following supporting information can be downloaded at: https://www.mdpi.com/article/10.3390/en18010034/s1, Table S1: Comparison of materials and properties in related research work [32,34,35,37,45,46]. Figure S1: SEM images of Bulk MoS_2; Figure S2: SEM and EDS mapping images of $MoS_2 \cdot H_2O$; Figure S3: SEM and EDS mapping images of MoS_2-PEDOT; Figure S4: SEM images of H-MoS_2-PEDOT, MoS_2-PEDOT and $MoS_2 \cdot H_2O$ At the same magnification; Figure S5: XPS images of S 2p; Figure S6: Electrochemical cycle curves measured at 0.1 A g^{-1}; Figure S7: GITT curves of H-MoS_2-PEDOT and MoS_2-PEDOT; Figure S8: Ex-situ SEM images of H-MoS_2-PEDOT. Figure S9: The pore size distributions of the H-MoS_2-PEDOT.

Author Contributions: T.J. and S.L. were responsible for manuscript conceptualization, methodology, and writing—original draft preparation. Z.L. was responsible for formal analysis, supervision, and project administration. X.L. (Xue Li) and L.Z. were responsible for resource provision and funding acquisition. H.S. was responsible for resource provision, funding acquisition, and writing—review and editing. X.L. (Xin Li) was responsible for resource provision and funding acquisition. Y.M. was responsible for writing—reviewing and editing. All authors have read and agreed to the published version of the manuscript.

Funding: This work was funded by the National Key Research and Development Program of China (No. 2022YFB1903200), the National Natural Science Foundation of China (Nos. 12175190 and U2241284), the Natural Science Foundation of Fujian Province China (No. 2022J02006), the Basic and Applied Basic Research Foundation of Guangdong Province, China (No. 2024A1515012156).

Data Availability Statement: The raw data supporting the conclusions of this article will be made available by the authors upon request.

Conflicts of Interest: The authors declare no conflicts of interest.

References

1. Aizudin, M.; Fu, W.; Pottammel, R.P.; Dai, Z.; Wang, H.; Rui, X.; Zhu, J.; Li, C.C.; Wu, X.L.; Ang, E.H. Recent Advancements of Graphene-Based Materials for Zinc-Based Batteries: Beyond Lithium-Ion Batteries. *Small* **2023**, *20*, 2305217. [CrossRef] [PubMed]
2. Degen, F.; Winter, M.; Bendig, D.; Tübke, J. Energy consumption of current and future production of lithium-ion and post lithium-ion battery cells. *Nat. Energy* **2023**, *8*, 1284–1295. [CrossRef]
3. Ji, G.; Wang, J.; Liang, Z.; Jia, K.; Ma, J.; Zhuang, Z.; Zhou, G.; Cheng, H.-M. Direct regeneration of degraded lithium-ion battery cathodes with a multifunctional organic lithium salt. *Nat. Commun.* **2023**, *14*, 584. [CrossRef] [PubMed]
4. Liu, Y.K.; Zhao, C.Z.; Du, J.; Zhang, X.Q.; Chen, A.B.; Zhang, Q. Research Progresses of Liquid Electrolytes in Lithium-Ion Batteries. *Small* **2022**, *19*, e2205315. [CrossRef] [PubMed]

5. Quilty, C.D.; Wu, D.; Li, W.; Bock, D.C.; Wang, L.; Housel, L.M.; Abraham, A.; Takeuchi, K.J.; Marschilok, A.C.; Takeuchi, E.S. Electron and Ion Transport in Lithium and Lithium-Ion Battery Negative and Positive Composite Electrodes. *Chem. Rev.* **2023**, *123*, 1327–1363. [CrossRef]
6. Tian, J.; Fan, Y.; Pan, T.; Zhang, X.; Yin, J.; Zhang, Q. A critical review on inconsistency mechanism, evaluation methods and improvement measures for lithium-ion battery energy storage systems. *Renew. Sustain. Energy Rev.* **2024**, *189*, 113978. [CrossRef]
7. Zheng, Y.; Che, Y.; Hu, X.; Sui, X.; Stroe, D.-I.; Teodorescu, R. Thermal state monitoring of lithium-ion batteries: Progress, challenges, and opportunities. *Prog. Energy Combust. Sci.* **2024**, *100*, 101120. [CrossRef]
8. Kakarla, A.K.; Bandi, H.; Syed, W.A.; Shanthappa, R.; Yu, J.S. Structural engineering of potassium vanadate cathode by pre-intercalated Mg^{2+} for high-performance and durable rechargeable aqueous zinc-ion batteries. *J. Magnes. Alloys* **2024**, *12*, 3780–3793. [CrossRef]
9. Ding, Z.; Jiang, T.; Zhao, W.; Luo, Z.; San, H.; Li, S.; Li, X.; Zhang, L. Photo-rechargeable zinc-ion battery using highly ordered and vertically oriented C@ VO_2/ZnO microrod arrays. *Energy Storage Mater.* **2024**, *71*, 103646. [CrossRef]
10. Kakarla, A.K.; Bandi, H.; Syed, W.A.; Narsimulu, D.; Shanthappa, R.; Yu, J.S. Unraveling Energy Storage Performance and Mechanism of Metal–Organic Framework-Derived Copper Vanadium Oxides with Tunable Composition for Aqueous Zinc-Ion Batteries. *Small Methods* **2024**, e2400819. (Online ahead of print). [CrossRef]
11. Nie, C.; Wang, G.; Wang, D.; Wang, M.; Gao, X.; Bai, Z.; Wang, N.; Yang, J.; Xing, Z.; Dou, S. Recent Progress on Zn Anodes for Advanced Aqueous Zinc-Ion Batteries. *Adv. Energy Mater.* **2023**, *13*, 2300606. [CrossRef]
12. Ding, Z.; Luo, Z.; San, H.; Li, X.; Zhang, L. Betavoltaic rechargeable Zn-ion battery based on hybrid cathode by combining betavoltaic structure with intercalation host. *Appl. Phys. Lett.* **2024**, *125*, 233901. [CrossRef]
13. Bandi, H.; Kakarla, A.K.; Dahule, R.; Maezono, R.; Narsimulu, D.; Shanthappa, R.; Yu, J.S. Nickel Vanadate Cathode Induced In Situ Phase Transition for Improved Zinc Storage by Low Migration Barrier and Zn^{2+}/H^+ Co-Insertion Mechanism. *Small* **2024**, e2408568. (Online ahead of print). [CrossRef] [PubMed]
14. Ding, Z.; Jiang, T.; Zheng, R.; Wang, N.; Zhang, L.; Liu, S.; Li, X.; San, H. Quantitative modeling, optimization, and verification of ^{63}Ni-powered betavoltaic cells based on three-dimensional ZnO nanorod arrays. *Nucl. Sci. Tech.* **2022**, *33*, 144. [CrossRef]
15. Syed, W.A.; Kakarla, A.K.; Bandi, H.; Shanthappa, R.; Yu, J.S. Copper substituted manganese Prussian blue analogue composite nanostructures for efficient aqueous zinc-ion batteries. *J. Energy Storage* **2024**, *99*, 113325. [CrossRef]
16. Guo, C.; Yi, S.; Si, R.; Xi, B.; An, X.; Liu, J.; Li, J.; Xiong, S. Advances on Defect Engineering of Vanadium-Based Compounds for High-Energy Aqueous Zinc–Ion Batteries. *Adv. Energy Mater.* **2022**, *12*, 2202039. [CrossRef]
17. Gao, N.; Song, Y.; Li, C.; Hu, C. Effect of MnO_2 Morphology on Kinetics and Stability in Zinc-Ion Batteries. *ACS Appl. Mater. Interfaces* **2023**, *15*, 28044–28054. [CrossRef]
18. Li, C.; Hu, C.; Song, Y.; Gao, N.; Yang, W.; Xu, X. Microfluidic-oriented assembly of Mn_3O_4@C/GFF cathode with multiscale synergistic structure for high-performance aqueous zinc-ion batteries. *Carbon* **2023**, *208*, 247–254. [CrossRef]
19. Zhang, J.; Li, W.; Wang, J.; Pu, X.; Zhang, G.; Wang, S.; Wang, N.; Li, X. Engineering p-Band Center of Oxygen Boosting H+ Intercalation in δ-MnO_2 for Aqueous Zinc Ion Batteries. *Angew. Chem. Int. Ed.* **2023**, *62*, e202215654. [CrossRef]
20. Liu, S.; Ding, Z.; Jiang, T.; Chi, T.; San, H.; Cui, J.; Liu, S.; Li, X.; Li, X.; Zhang, L. Photo-rechargeable lithium-ions batteries based on V_2O_5 nanorods/TiO_2 heterostructure. *J. Energy Storage* **2024**, *84*, 110822. [CrossRef]
21. Deng, S.; Li, H.; Chen, B.; Xu, Z.; Jiang, Y.; Li, C.; Xiao, W.; Yan, X. High performance of Mn-doped VO_2 cathode for aqueous zinc-ion batteries: An insight into Zn^{2+} storage mechanism. *Chem. Eng. J.* **2023**, *452*, 139115. [CrossRef]
22. Gu, X.; Wang, J.; Zhao, X.; Jin, X.; Jiang, Y.; Dai, P.; Wang, N.; Bai, Z.; Zhang, M.; Wu, M. Engineered nitrogen doping on VO_2(B) enables fast and reversible zinc-ion storage capability for aqueous zinc-ion batteries. *J. Energy Chem.* **2023**, *85*, 30–38. [CrossRef]
23. Chen, X.; Kong, Q.; Wu, X.; An, X.; Zhang, J.; Wang, Q.; Yao, W. V_2O_3@C optimized by carbon regulation strategy for ultra long-life aqueous zinc-ion batteries. *Chem. Eng. J.* **2023**, *451*, 138765. [CrossRef]
24. Ding, Y.L.; Kopold, P.; Hahn, K.; van Aken, P.A.; Maier, J.; Yu, Y. A Lamellar Hybrid Assembled from Metal Disulfide Nanowall Arrays Anchored on a Carbon Layer: In Situ Hybridization and Improved Sodium Storage. *Adv. Mater.* **2016**, *28*, 7774–7782. [CrossRef] [PubMed]
25. Liu, Y.; Zhang, N.; Kang, H.; Shang, M.; Jiao, L.; Chen, J. WS_2 Nanowires as a High-Performance Anode for Sodium-Ion Batteries. *Chem.—A Eur. J.* **2015**, *21*, 11878–11884. [CrossRef]
26. Liu, W.; Hao, J.; Xu, C.; Mou, J.; Dong, L.; Jiang, F.; Kang, Z.; Wu, J.; Jiang, B.; Kang, F. Investigation of zinc ion storage of transition metal oxides, sulfides, and borides in zinc ion battery systems. *Chem. Commun.* **2017**, *53*, 6872–6874. [CrossRef]
27. Zhao, C.; Yu, C.; Zhang, M.; Sun, Q.; Li, S.; Norouzi Banis, M.; Han, X.; Dong, Q.; Yang, J.; Wang, G. Enhanced sodium storage capability enabled by super wide-interlayer-spacing MoS_2 integrated on carbon fibers. *Nano Energy* **2017**, *41*, 66–74. [CrossRef]
28. Jia, X.; Liu, C.; Neale, Z.G.; Yang, J.; Cao, G. Active materials for aqueous zinc ion batteries: Synthesis, crystal structure, morphology, and electrochemistry. *Chem. Rev.* **2020**, *120*, 7795–7866. [CrossRef]
29. Xu, W.; Sun, C.; Zhao, K.; Cheng, X.; Rawal, S.; Xu, Y.; Wang, Y. Defect engineering activating (Boosting) zinc storage capacity of MoS_2. *Energy Storage Mater.* **2019**, *16*, 527–534. [CrossRef]

30. Lv, R.; Robinson, J.A.; Schaak, R.E.; Sun, D.; Sun, Y.; Mallouk, T.E.; Terrones, M. Transition Metal Dichalcogenides and Beyond: Synthesis, Properties, and Applications of Single- and Few-Layer Nanosheets. *Acc. Chem. Res.* **2015**, *48*, 56–64. [CrossRef]
31. Liu, J.; Xu, P.; Liang, J.; Liu, H.; Peng, W.; Li, Y.; Zhang, F.; Fan, X. Boosting aqueous zinc-ion storage in MoS_2 via controllable phase. *Chem. Eng. J.* **2020**, *389*, 124405. [CrossRef]
32. Liang, H.; Cao, Z.; Ming, F.; Zhang, W.; Anjum, D.H.; Cui, Y.; Cavallo, L.; Alshareef, H.N. Aqueous Zinc-Ion Storage in MoS_2 by Tuning the Intercalation Energy. *Nano Lett.* **2019**, *19*, 3199–3206. [CrossRef] [PubMed]
33. Zhou, M.; Cheng, L.; Han, B.; Zhang, H.; Chen, J.; Xie, F.; Wang, N.; Jin, Y.; Meng, H. Cobalt-doped molybdenum disulfide with rich defects and extended layered structure for rechargeable zinc-ion batteries. *J. Alloys Compd.* **2022**, *916*, 165487. [CrossRef]
34. Liu, F.; Li, L.; Xu, S.; Guo, J.; Ling, Y.; Zhang, Y.; Gong, W.; Wei, L.; Wang, C.; Zhang, Q.; et al. Cobalt-doped $MoS_2{\cdot}nH_2O$ nanosheets induced heterogeneous phases as high-rate capability and long-term cyclability cathodes for wearable zinc-ion batteries. *Energy Storage Mater.* **2023**, *55*, 1–11. [CrossRef]
35. Yang, W.; Mou, L.; Xiao, B.; Chen, J.; Wang, D.; Peng, S.; Huang, J. Mn^{2+}-Doped MoS_2/MXene Heterostructure Composites as Cathodes for Aqueous Zinc-Ion Batteries. *ACS Appl. Mater. Interfaces* **2023**, *15*, 51231–51240. [CrossRef]
36. Li, S.; Wei, X.; Wu, C.; Zhang, B.; Wu, S.; Lin, Z. Constructing Three-Dimensional Structured V_2O_5/Conductive Polymer Composite with Fast Ion/Electron Transfer Kinetics for Aqueous Zinc-Ion Battery. *ACS Appl. Energy Mater.* **2021**, *4*, 4208–4216. [CrossRef]
37. Lv, Z.; Tan, Y.; Kang, Y.; Yang, J.; Cheng, X.; Meng, W.; Zhang, Y.; Li, C.C.; Zhao, J.; Yang, Y. Non-desolvation Zn^{2+} storage mechanism enables MoS_2 anode with enhanced interfacial charge-transfer kinetics for low temperature zinc-ion batteries. *Sci. China Chem.* **2023**, *66*, 1537–1548. [CrossRef]
38. Elia, G.A.; Greco, G.; Kamm, P.H.; García-Moreno, F.; Raoux, S.; Hahn, R. Simultaneous X-Ray Diffraction and Tomography Operando Investigation of Aluminum/Graphite Batteries. *Adv. Funct. Mater.* **2020**, *30*, 2003913. [CrossRef]
39. Reddy Inta, H.; Biswas, T.; Ghosh, S.; Kumar, R.; Kanti Jana, S.; Mahalingam, V. Ionic Liquid-Intercalated Metallic MoS_2 as a Superior Electrode for Energy Storage Applications. *ChemNanoMat* **2020**, *6*, 685–695. [CrossRef]
40. He, H.; Luo, Z.; Liu, Z.; Zhang, Z.; Chen, Y.; Deng, Q.; Chen, X.; Chen, W.; Zeng, J. Understanding the partial substitution effect of Mg in Zn-V aqueous batteries. *J. Electroanal. Chem.* **2023**, *929*, 117094. [CrossRef]
41. Zhang, T.; Feng, Y.; Zhang, J.; He, C.; Itkis, D.M.; Song, J. Ultrahigh-rate sodium-ion battery anode enabled by vertically aligned (1T-2H MoS_2)/CoS_2 heteronanosheets. *Mater. Today Nano* **2020**, *12*, 100089. [CrossRef]
42. Kang, C.W.; Park, J.; Kim, G.H.; Ko, K.C.; Son, S.U. Hexagonal Carbon Nanoplates Decorated with Layer-Engineered MoS_2: High-Performance Cathode Materials for Zinc-Ion Batteries. *ACS Appl. Mater. Interfaces* **2023**, *15*, 7887–7898. [CrossRef] [PubMed]
43. Chen, H.-W.; Li, C. PEDOT: Fundamentals and Its Nanocomposites for Energy Storage. *Chin. J. Polym. Sci.* **2019**, *38*, 435–448. [CrossRef]
44. Li, S.; Wei, Y.; Wu, Q.; Han, Y.; Qian, G.; Liu, J.; Yang, C. Super p/MoS_2 cathode material for aqueous zinc-ion batteries. *Ionics* **2023**, *30*, 229–236. [CrossRef]
45. Liu, H.; Wang, J.-G.; Hua, W.; You, Z.; Hou, Z.; Yang, J.; Wei, C.; Kang, F. Boosting zinc-ion intercalation in hydrated MoS_2 nanosheets toward substantially improved performance. *Energy Storage Mater.* **2021**, *35*, 731–738. [CrossRef]
46. Li, S.; Liu, Y.; Zhao, X.; Shen, Q.; Zhao, W.; Tan, Q.; Zhang, N.; Li, P.; Jiao, L.; Qu, X. Sandwich-like heterostructures of MoS_2/graphene with enlarged interlayer spacing and enhanced hydrophilicity as high-performance cathodes for aqueous zinc-ion batteries. *Adv. Mater.* **2021**, *33*, 2007480. [CrossRef]